Mon. Not. R. Astron. Soc. **308,** 289–301 (1999)

The power spectrum of the Point Source Catalogue redshift survey

W. Sutherland,[1⋆] H. Tadros,[1,2] G. Efstathiou,[3] C. S. Frenk,[4] O. Keeble,[5] S. Maddox,[3] R. G. McMahon,[3] S. Oliver,[5] M. Rowan-Robinson,[5] W. Saunders[6] and S. D. M. White[7]

[1]*Department of Physics, Keble Road, Oxford OX1 3RH*
[2]*Astronomy Centre, University of Sussex, Brighton BN1 9QH*
[3]*Institute of Astronomy, Madingley Road, Cambridge CB3 0HA*
[4]*Department of Physics, South Road, Durham DH1 3LE*
[5]*Astrophysics Group, Imperial College, Blackett Laboratory, Prince Consort Road, London SW7 2BZ*
[6]*Royal Observatory, Blackford Hill, Edinburgh EH9 3HJ*
[7]*Max-Planck-Institut für Astrophysik, Karl-Schwarzschild-Strasse 1, D-8046 Garching bei Munchen, Germany*

Accepted 1999 January 19. Received 1999 January 19; in original form 1998 August 10

ABSTRACT

We measure the redshift-space power spectrum $P(k)$ for the recently completed *IRAS* Point Source Catalogue (PSC) redshift survey, which contains 14 500 galaxies over 84 per cent of the sky with 60-μm flux $\geq$0.6 Jy. Comparison with simulations shows that our estimated errors on $P(k)$ are realistic, and that systematic errors resulting from the finite survey volume are small for wavenumbers $k \gtrsim 0.03\,h\,\mathrm{Mpc}^{-1}$. At large scales our power spectrum is intermediate between those of the earlier QDOT and 1.2-Jy surveys, but with considerably smaller error bars; it falls slightly more steeply to smaller scales. We have fitted families of CDM-like models using the Peacock–Dodds formula for non-linear evolution; the results are somewhat sensitive to the assumed small-scale velocity dispersion σ_V. Assuming a realistic $\sigma_V \approx 300\,\mathrm{km\,s}^{-1}$ yields a shape parameter $\Gamma \sim 0.25$ and normalization $b\sigma_8 \sim 0.75$; if σ_V is as high as $600\,\mathrm{km\,s}^{-1}$ then $\Gamma = 0.5$ is only marginally excluded. There is little evidence for any 'preferred scale' in the power spectrum or non-Gaussian behaviour in the distribution of large-scale power.

Key words: surveys – galaxies: distances and redshifts – large-scale structure of Universe.

1 INTRODUCTION

As is well known (e.g. Peebles 1980), the power spectrum of the galaxy distribution on large scales is of great importance for testing cosmological models, since it can be related to the initial conditions by linear perturbation theory. The power spectrum has been estimated from a variety of galaxy redshift surveys, notably the CfA redshift survey (Park et al. 1994), the QDOT survey (Feldman, Kaiser & Peacock 1994, hereafter FKP), the Las Campanas redshift survey (Lin et al. 1996), and the 1.2-Jy *IRAS* survey (Fisher et al. 1993). Also, the real-space power spectrum has been inferred from the APM Galaxy Survey (Baugh & Efstathiou 1993; Baugh & Efstathiou 1994a) by inversion of both the angular correlation function and the 2D power spectrum.

Despite these substantial surveys, there are still considerable uncertainties in the shape of the power spectrum on large scales, since most of these surveys contain only a small number of independent structures, while the largest one (Las Campanas) has a slice-like geometry which complicates the estimation of the power spectrum. If the primordial power spectrum is $P(k) \propto k^n$ with $n \approx 1$ as suggested by inflation, then for consistency with the *COBE* DMR results the present-day power spectrum must show a turn-over to this slope at $k \lesssim 0.02\,h\,\mathrm{Mpc}^{-1}$, close to the largest scales accessible to current galaxy surveys. There is marginal evidence for such a turn-over in the APM data (Baugh & Efstathiou 1994a; Maddox, Efstathiou & Sutherland 1996; Tadros, Efstathiou & Dalton 1998).

Also, it is valuable to measure the power spectrum from surveys with different selection criteria (e.g. optical and *IRAS* selection). This is of considerable interest since the observed power spectrum is measured from the density field of galaxies, whereas theory predicts the power spectrum of the mass distribution. The process of galaxy formation is poorly understood, so the observed $P_\mathrm{g}(k)$ may differ from $P_\mathrm{m}(k)$, possibly in a complex way; indeed, since it appears that *IRAS* galaxies and optical galaxies have different small-scale correlation amplitudes, at least one of these cannot trace the mass. A simple 'linear bias' model is often assumed, in which $\delta_\mathrm{g} = b\delta_\mathrm{m}$ for some constant 'bias factor' b which may depend on galaxy type; this model predicts that $P(k)$ for optical and *IRAS* galaxies should differ by a multiplicative factor of $(b_\mathrm{O}/b_\mathrm{I})^2$. Such a model is reasonable since it has been shown by several authors (e.g. Fry & Gaztanaga 1993; Cole et al. 1998; Mann, Peacock & Heavens 1998) that if the galaxy density is a (possibly

⋆Visiting Observer, Cerro Tololo Interamerican Observatory.

complex and stochastic) function only of the *local* mass density on scales $\lesssim 1\,h^{-1}$ Mpc, then the effective bias parameter defined by $b(r) \equiv \sqrt{\xi_{\rm g}(r)/\xi_{\rm m}(r)}$ tends to a constant on large scales, so such a 'local' bias cannot alter the large-scale shape of the power spectrum.

Another motivation for measuring the power spectrum from a large sample of *IRAS* galaxies is that there appears to be a marginal discrepancy between the power spectra from the previous QDOT (FKP) and 1.2-Jy (Fisher et al. 1993) *IRAS* surveys, with the amplitude of $P(k)$ from QDOT being roughly a factor of 2 higher at large scales. A counts-in-cells comparison of the two surveys does not reveal any obvious systematic errors (Efstathiou 1995), but it is interesting to check whether these differences are consistent with sampling fluctuations in one or both surveys.

In this paper, we estimate the redshift-space power spectrum from a new redshift survey (Saunders et al. 1996) of some 14 500 galaxies over 84 per cent of the sky, selected at 60 μm from the *IRAS* Point Source Catalogue (PSC). A variety of analyses from this survey will appear shortly; the topology of the density field has been analysed by Canavezes et al. (1998), the correlation function is analysed by Maddox et al. (in preparation), the dipole is estimated by Rowan-Robinson et al. (in preparation), a reconstruction of the peculiar velocity field is given by Branchini et al. (1999), and the redshift-space distortions are estimated using spherical harmonics by Tadros et al. (1999).

The plan of this paper is as follows: in Section 2 we summarize the construction and properties of the survey; in Section 3 we present the power spectrum estimates, and we compare these with results of N-body simulations in Section 4. In Section 5 we compare our results with other surveys and some parametrized cosmological models, and also set limits on non-Gaussian behaviour and periodicities.

2 THE PSC REDSHIFT SURVEY

The construction of the PSC redshift survey (hereafter PSCz) is described in detail elsewhere (Saunders et al. 1996; Saunders et al. in preparation), but we summarize the main points here. The aim of the survey is to obtain redshifts for all galaxies with 60-μm flux $f_{60} > 0.6$ Jy over as much of the sky as feasible. The starting point for the survey is the QMW *IRAS* Galaxy Catalogue (Rowan-Robinson et al. 1991), but with modifications to extend the sky coverage and improve completeness. We have relaxed the *IRAS* colour criteria for galaxy selection, and we have added in additional sources in the '2-HCON' sky as follows: the *IRAS* satellite covered most of the sky with 3 hours-confirmed scans (HCONs) (Beichman et al. 1988), while about 20 per cent of the sky had only 2 HCONs. Since a source must be detected in 2 separate HCONS for inclusion, the PSC catalogue may be less complete in the 2-HCON regions. Thus, in the 2-HCON sky we added sources to our target list which had a 1-HCON detection in the 'Point Source Reject' file and also had a matching entry in the *IRAS* Faint Source Catalogue.

These relaxed selection criteria allowed more contamination of the target list by non-galaxy sources, but these were excluded using APM or COSMOS scans of the POSS and UKST sky survey plates. If the APM or COSMOS data showed no 'obvious' galaxy candidate near the *IRAS* source, we visually inspected the plate and attempted to classify the source, rejecting it if it showed an obvious Galactic counterpart, e.g. an H II region, planetary nebula, dark cloud etc. We also exclude very faint galaxies ($B_{\rm J} > 19.5$) from the redshift survey since measuring their redshifts is time-consuming, and they are usually at $z > 0.1$ and hence have little effect on most of the desired analyses.

The sky coverage of the survey is the whole sky, excluding areas with less than 2 HCONs in the *IRAS* data, regions with optical extinction $A_V > 1.42$ mag as estimated from the *IRAS* 100-μm maps and two small areas near the Large and Small Magellanic Clouds. The resulting coverage is 84 per cent of the whole sky. (An extension to 93 per cent sky coverage is in progress, using a combination of K-band snapshots and H I redshifts).

Our 2D source catalogue contains 17 060 *IRAS* sources in the unmasked sky. Of these, 1593 are rejected as objects in our own Galaxy (e.g. cirrus, bright stars, reflection nebulae, planetary nebulae etc.), or as multiple entries from very nearby galaxies 'broken up' by the *IRAS* point source detection scheme. Another 648 sources are rejected either as very faint galaxies (~400) or as sources without an optical identification. This leaves 14 819 galaxies in the 'target' list, and redshifts are now known for 14 539 of these (98 per cent).

Of these redshifts, ~6500 are from a combination of the 1.2-Jy survey (Fisher et al. 1994) and QDOT (Lawrence et al. 1998), and ~3000 are from other publications and private communications. A further 4115 redshifts were measured by us for this survey, using 49 nights at the Isaac Newton Telescope, 18 nights at the Cerro Tololo 1.5-m telescope, and 6 nights at the Anglo-Australian Telescope, between 1992 January and 1995 July. Details of the observations and data reduction will be given elsewhere (Saunders et al., in preparation). The error on our redshifts is typically $150\,{\rm km\,s^{-1}}$; for the literature redshifts it is somewhat smaller. The median redshift of the sample is $\approx 8500\,{\rm km\,s^{-1}}$, though there is a long 'tail' extending to $> 30\,000\,{\rm km\,s^{-1}}$ because of the broad luminosity function of *IRAS* galaxies.

3 POWER SPECTRUM ESTIMATION

For the estimates here, we restrict the analysis to the unmasked sky with the additional constraint $|b| > 10°$, since the survey may be slightly incomplete below this latitude; this gives a coverage of 78 per cent of the full sky. We also set an upper redshift limit of $cz < 45\,000\,{\rm km\,s^{-1}}$, since the survey is incomplete at high redshift as noted above. This gives 13 346 galaxies in the 'default' sample used for the power spectrum estimate.

Since the geometry of the survey is well approximated by a sphere, apart from the missing slice near the Galactic plane, we follow the analysis of FKP with minor modifications. This method provides an optimal weighting scheme with redshift for estimating the power spectrum of an all-sky survey. More sophisticated methods have been suggested by e.g. Tegmark (1995) and Tegmark et al. (1998); these are very useful for surveys with highly non-spherical geometries but are more complex than necessary for our survey.

We convert the galaxy positions to comoving coordinates assuming $\Omega_0 = 1$ and redshifts in the Local Group frame, and bin the galaxies in a cube of size $950\,h^{-1}$ Mpc with 128^3 cells. The FKP method assigns a redshift-dependent weight to each object,

$$w(r) = \frac{1}{\sqrt{A}[1 + P_{\rm e}\overline{n}(r)]} \tag{1}$$

where $\overline{n}(r)$ is the mean galaxy density at distance r, $P_{\rm e}$ is the estimated power spectrum (at some scale to be determined), and A is a normalization constant (see later). We use a parametric fit for the selection function determined using the method of Springel & White (1998); here this takes the form

$$\begin{aligned} &\overline{n}(z) = n_* y^{(1-\alpha)}/(1+y^{\gamma})^{(\beta/\gamma)}, \\ &\quad y \equiv z/z_*, \qquad z_* = 0.0318, \\ &\quad \alpha = 1.769, \qquad \beta = 4.531, \qquad \gamma = 1.335, \\ &\quad n_* = 8.76\times 10^{-3}\,h^3\,{\rm Mpc}^{-3}; \end{aligned} \tag{2}$$

these values are appropriate for $f \geq 0.6$ Jy; for other flux limits we simply scale z_* by $\sqrt{(0.6/f_{\rm lim})}$.

We have made three refinements to the FKP estimator: first, we define the ratio of densities of real and random catalogues $\alpha' = \sum_{\rm g} w_i / \sum_{\rm s} w_j$, where w_i is the weight of the ith object and the sums run over galaxies and random points respectively (Tadros & Efstathiou 1996), instead of $\alpha = N_{\rm g}/N_{\rm r}$ as in FKP (where $N_{\rm g}, N_{\rm r}$ are the numbers of galaxies and random points respectively). Secondly, we compute the shot noise using

$$P_{\rm shot} = \sum_{\rm g} w_i^2 + \alpha'^2 \sum_{\rm s} w_j^2, \tag{3}$$

where the two terms are the contributions from galaxies and random points respectively. The shot noise definition in FKP's equation (2.4.5) was $P_{\rm shot} = \alpha(1+\alpha)\sum_{\rm s} w_j^2$; there the first-order term in α is the 'expected' shot noise from the galaxies given many realizations of the given selection function, while the first term in our definition is the 'actual' shot noise in the data. This makes negligible difference at large scales, but we find from simulations that equation (3) gives substantially smaller errors in the estimated power spectrum at small scales (large k), because the shot noise term is substantial here and the 'actual' shot noise from the galaxies may differ significantly from its expectation value estimated from the selection function.

The third refinement is that we use a normalization convention given by equation (A3); see Appendix A for a discussion of the normalization.

The estimated power spectrum $\widehat{P}(k)$ is then given as in FKP, by

$$F(\boldsymbol{r}) = w(r)[n_{\rm g}(\boldsymbol{r}) - \alpha' n_{\rm s}(\boldsymbol{r})], \tag{4}$$

$$F(\boldsymbol{k}) = \int {\rm d}^3 r\, F(\boldsymbol{r}) {\rm e}^{i\boldsymbol{k}.\boldsymbol{r}}, \tag{5}$$

$$\widehat{P}(\boldsymbol{k}) = |F(\boldsymbol{k})|^2 - P_{\rm shot}, \tag{6}$$

where $n_{\rm g}, n_{\rm s}$ are the number densities of galaxies and random points in cubical cells, and $\widehat{P}(k)$ is just the unweighted average of $\widehat{P}(\boldsymbol{k})$ over a spherical shell with mean radius k.

The optimal weighting scheme depends on the actual value of $P(k)$, so the procedure is slightly circular in principle. We have used values of $P_{\rm e} = 2000, 4000, 8000, 16\,000\,h^{-3}\,{\rm Mpc}^3$; estimates of the power spectrum for each value of $P_{\rm e}$ are shown in Fig. 1.

We see that changing $P_{\rm e}$ changes the size of the error bars, but there is little systematic difference in the resulting estimates of $\widehat{P}(k)$. This is as expected since FKP showed that any choice of $P_{\rm e}$ gives an unbiased estimate of $P(k)$ (apart from the convolution effects at small k discussed below), but just weights different redshift shells differently – larger $P_{\rm e}$ gives relatively more weight to more distant shells. We adopt $P_{\rm e} = 8000\,h^{-3}\,{\rm Mpc}^3$ as the default value for the remainder of the paper. The resulting weights are illustrated in Fig. 2: the solid line shows the weight function $w(z)$, and the dotted line shows the real-space window function $\overline{n}(z)w(z)$. Also shown are the differential and cumulative contributions to the survey 'effective volume' per unit redshift.

We have explored varying many of the selection criteria, e.g. varying the model of the selection function, using a maximum redshift of $30\,000\,{\rm km\,s^{-1}}$, or a galactic latitude cut of 20^o, and changing the flux threshold. Most of these changes have a negligible effect on the results, with the exception of changing the flux limit: the subsample with $f_{60} > 0.8$ Jy has a slightly lower amplitude of $\widehat{P}(k)$ at all scales; the difference is mostly within the individual 1σ error bars but is evident over a range of k. The slice with $0.6 < f_{60} < 0.8$ Jy has correspondingly higher amplitude. This might be suggestive of systematic errors in the catalogue near the flux limit, as suggested by Hamilton (1996); however we have investigated the correlation function $\xi(\sigma, \pi)$ as a function of projected and redshift separation and find negligible evidence for a 'Hamilton effect' i.e. elongation of the correlation function out to large redshift separation. The correlation functions of the subsamples above and below 0.8 Jy show a similar difference in amplitudes to the $\widehat{P}(k)$s, but the difference is most pronounced at small to intermediate scales, rather than at large scales as might be expected from systematic errors; thus this effect may be a sampling

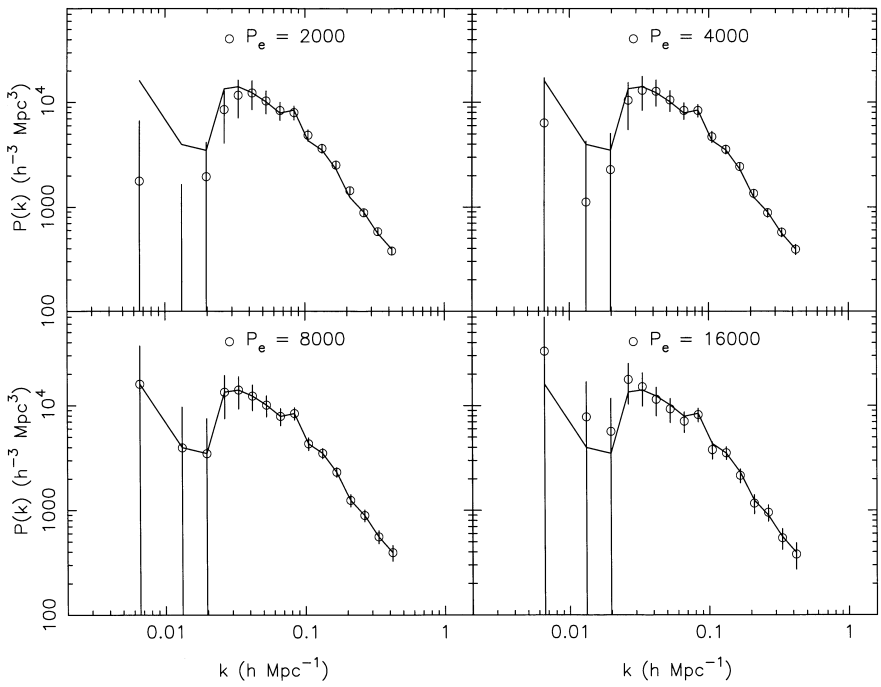

Figure 1. Estimated redshift-space power spectra $\widehat{P}(k)$ for weights $P_{\rm e} = 2000, 4000, 8000, 16\,000\,h^{-3}\,{\rm Mpc}^3$. Open circles with error bars show the result for each weight, while the solid line is the result for $P_{\rm e} = 8000\,h^{-3}{\rm Mpc}^3$ (the same in all panels).

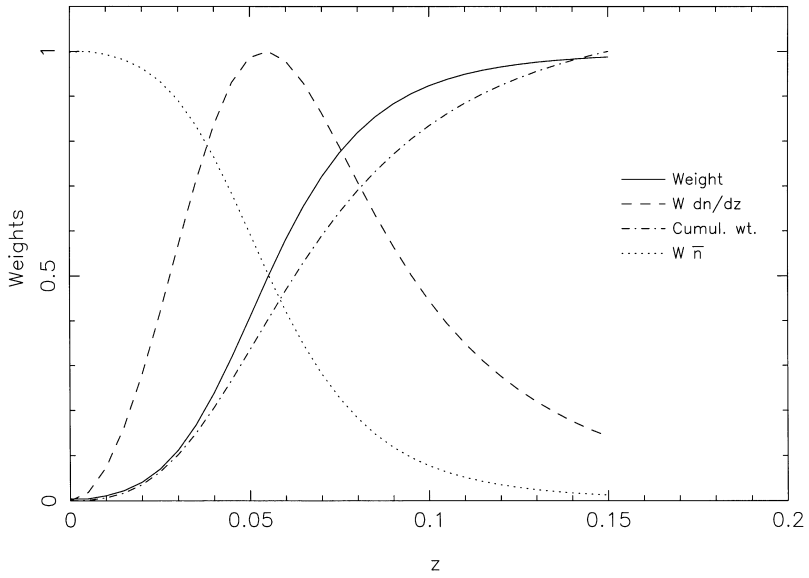

Figure 2. Weight and window functions versus redshift for $P_e = 8000\,h^{-3}\,\mathrm{Mpc}^3$, in arbitrary units. The solid line shows the weight $w(z)$, and the dotted line shows the real-space window function $\bar{n}(z)w(z)$. The dashed line shows $\bar{n}(z)w(z)\mathrm{d}V/\mathrm{d}z$, i.e. the 'effective volume' of the survey per unit redshift, and the dot–dashed line is the integrated effective volume below redshift z.

fluctuation or possibly a dependence of clustering amplitude on intrinsic galaxy luminosity. Hereafter we use the full sample to 0.6 Jy with the caveat that the reason for this slight flux dependence is not yet clearly understood. The effect on the derived cosmological parameters in Section 5.2 is similar to or less than that resulting from the uncertainties arising from the small-scale velocity dispersion etc.

3.1 Observed versus true $P(k)$

As is well known, the finite size of the survey volume means that the estimated power spectrum is a convolution of the true power spectrum with the squared Fourier transform of the real-space window function; e.g. equations (2.1.6) and (2.1.10) of FKP give

$$\langle \widehat{P}(\boldsymbol{k})\rangle = (2\pi)^{-3}\int \mathrm{d}^3k'\,P(\boldsymbol{k}')|G(\boldsymbol{k}-\boldsymbol{k}')|^2, \tag{7}$$

$$G(\boldsymbol{r}) \equiv \bar{n}(\boldsymbol{r})w(\boldsymbol{r})\left[\int \mathrm{d}^3r\,\bar{n}^2(\boldsymbol{r})w^2(\boldsymbol{r})\right]^{-1/2},$$

and the normalization is defined so that

$$\int \mathrm{d}^3k\,|G(\boldsymbol{k})|^2 = (2\pi)^3 \tag{8}$$

by Parseval's theorem. This convolution is a significant problem for slice-like survey geometries with a highly anisotropic window function; but since our survey is large in all three dimensions, the window function is narrow. For our standard weighting with $P_e = 8000\,h^{-3}\,\mathrm{Mpc}^3$, the window function $|G(\boldsymbol{k})|^2$ is illustrated in Fig. 3 for three axes in Galactic coordinates, along

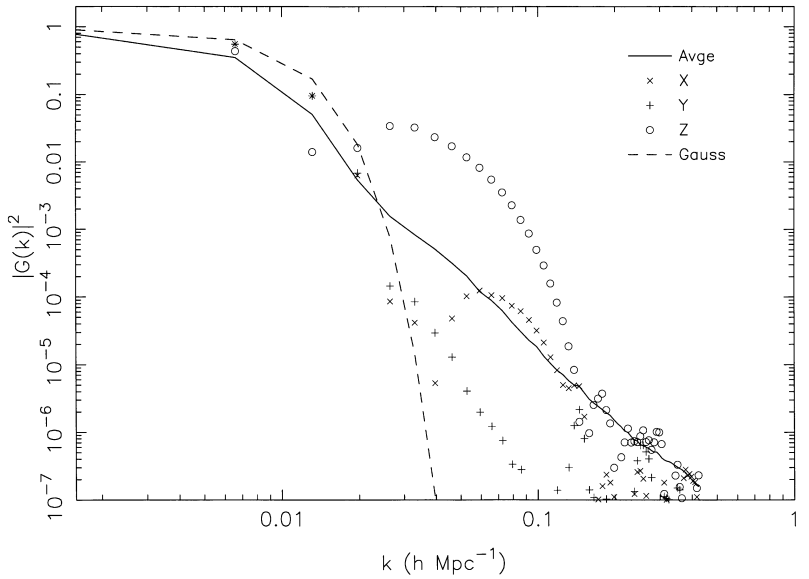

Figure 3. The k-space window function $|G(\boldsymbol{k})|^2$. Points show this quantity for $\boldsymbol{k}$ parallel to the Galactic x, y, z directions (as labelled). The solid line shows the direction-average over spherical shells of radius k. The dashed line shows a Gaussian $\exp(-k^2/2k_0^2)$ with $k_0 = 0.007\,h\,\mathrm{Mpc}^{-1}$ (this is for illustration and is not a fit).

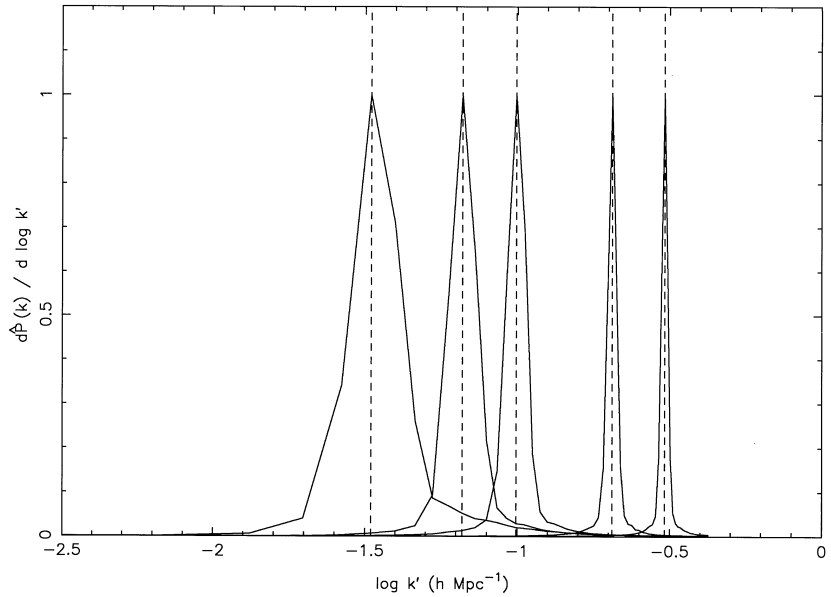

Figure 4. The effect of convolution, i.e. the contribution to 'observed' power $\widehat{P}(k)$ from 'true' wavenumber k' in equation (7), summed over directions of $\boldsymbol{k},\boldsymbol{k}'$, per unit $\ln k'$. Values are shown for observed $k = 0.033, 0.066, 0.1, 0.2, 0.3\,h\,\mathrm{Mpc}^{-1}$ (dashed lines). The y-scale is arbitrary.

with the angle-average. The window function is roughly approximated by a Gaussian $\exp(-k^2/2k_0^2)$ with $k_0 \sim 0.006\,h\,\mathrm{Mpc}^{-1}$ at small k, with a roughly k^{-4} tail arising from the survey mask. Therefore, the effect of the convolution on our estimates is small except at the largest scales $k \lesssim 0.03\,h\,\mathrm{Mpc}^{-1}$. This is illustrated in Fig. 4; the solid lines show the fractional contribution to the measured $\widehat{P}(k)$ as a function of 'true' wavenumber k', i.e. equation (7) averaged over directions of $\boldsymbol{k},\boldsymbol{k}'$ for five values of observed $k = 0.033, 0.066, 0.1, 0.2, 0.3\,h\,\mathrm{Mpc}^{-1}$, assuming a CDM-like model $P(k')$ with the parameter $\Gamma = 0.3$ (see equation 11 below). We have not attempted a deconvolution here, since the convolution effect is only important at small k where the estimates are becoming noisy.

Another effect which causes the measured $\widehat{P}(k)$ to deviate systematically from its true value is that the mean density of galaxies is not known independently but is estimated from the survey. This leads to the constraint $\widehat{P}(0) = 0$, and the convolution above means that $\widehat{P}(k)$ will also be underestimated for small but non-zero k. This effect was noted by Peacock & Nicholson (1991), and has been evaluated analytically by Tadros & Efstathiou (1996) for the special case of a volume-limited survey; their equation (A4.2) gives

$$\langle \widehat{P}(\boldsymbol{k}) - P(\boldsymbol{k}) \rangle \approx -\frac{\overline{n}}{V} |\widehat{W}(\boldsymbol{k})^2| - \overline{n}^2 \left[\sum_{\boldsymbol{k}'} |\widehat{W}(\boldsymbol{k}')|^2 P(\boldsymbol{k}') \right] |\widehat{W}(\boldsymbol{k})^2|. \quad (9)$$

For unequal weights as here, the expression is complex and best evaluated numerically; we have computed this for two models of $P(k)$: a $\Gamma = 0.3$ CDM model, and an $n = -1.2$ power law, with a bend to $n = 0$ at $k \leq 0.01\,h\,\mathrm{Mpc}^{-1}$. For each model, we generate a Gaussian random density field with the assumed $P(k)$, multiply by the PSCz window function $\overline{n}(r)w(r)$, set the mean of the windowed density field to zero, and compute the power spectrum of the resulting density field using the given $w(r)$. The mean of the recovered power spectra from 30 realizations of each model is shown in Fig. 5. We see that the bias is serious only for $k \lesssim 0.02\,h\,\mathrm{Mpc}^{-1}$; note in particular that for the power-law model the recovered power spectrum lies well above the PSCz measurements at $k \sim 0.01$–$0.03\,h\,\mathrm{Mpc}^{-1}$. The data points at $k \sim 0.013$ and $0.02\,h\,\mathrm{Mpc}^{-1}$ are noteworthy here; although their error bars appear large because of the logarithmic scale, none of the 30 realizations of the power-law model gave $\widehat{P}(k)$ as low as the PSCz data at these k.

Thus, we can be confident that the flattening of the observed power spectrum below $k \sim 0.06\,h\,\mathrm{Mpc}^{-1}$ is a real feature, not an artefact of the finite volume or normalization.

We compute the covariance matrix of $\widehat{P}(k)$ using equation (2.5.2) of FKP. In practice, it is infeasible to evaluate this directly since it contains $\sim N^6$ terms where $N = 128$; thus in practice, we assign each of the N^3 wavevectors to its bin in k; for each k, k' we pick $\sim 10^6$ random pairs of wavevectors $\boldsymbol{k},\boldsymbol{k}'$ in the appropriate bins, and evaluate the sum accordingly. It is found that $\sim 10^6$ pairs are necessary to ensure that the random errors are small, otherwise the resulting matrix can become non-positive-definite.

A final effect on $\widehat{P}(k)$ is the 'binning factor' noted by Baugh & Efstathiou (1994b), which causes an underestimate of small-scale power because of the galaxies being binned into finite-size cells before the Fourier transform. This 'smooths' the observed density field over the bin size. The size of this effect depends on the slope of the true power spectrum; a second-order approximation is given by equation (20) of Peacock & Dodds (1996), and is $\widehat{P}(k)/P(k) \approx \left[1 + (kl)^2/12\right]^{-1}$, where l is the size of the unit cells in the fast Fourier transform; this becomes inaccurate for $kl \gtrsim 2$. We find that for $n \sim -1$ a better approximation useful for $kl < \pi$ is

$$\widehat{P}(k)/P(k) \approx \left[1 + (kl)^2/12 - (kl)^4/220\right]^{-1}. \quad (10)$$

Since this correction is slightly model-dependent, we have not applied it to the estimates in Figs 1 or 6, but we have applied it before the model fitting in the following section and in Table 1.

4 COMPARISON WITH SIMULATIONS

As a check of the code, and to assess whether the resulting error bars are realistic, we have generated simulated 'PSCz' surveys from large N-body simulations from three cosmological models and

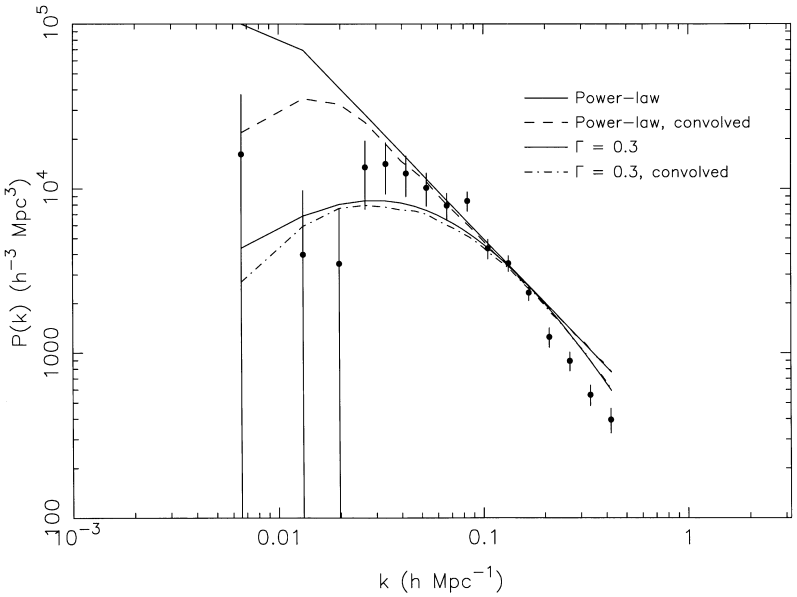

Figure 5. The effect of convolution and the normalization condition $\widehat{P}(k) = 0$ on two model power spectra (solid lines); the upper solid line shows a power law $P(k) \propto k^{-1.2}$ with a break at $k = 0.01\,h\,\mathrm{Mpc}^{-1}$; the lower solid line shows $\Gamma = 0.3$ CDM. The dashed and dot–dashed lines show the mean recovered power spectra for the two cases. Points show the measured values for PSCz.

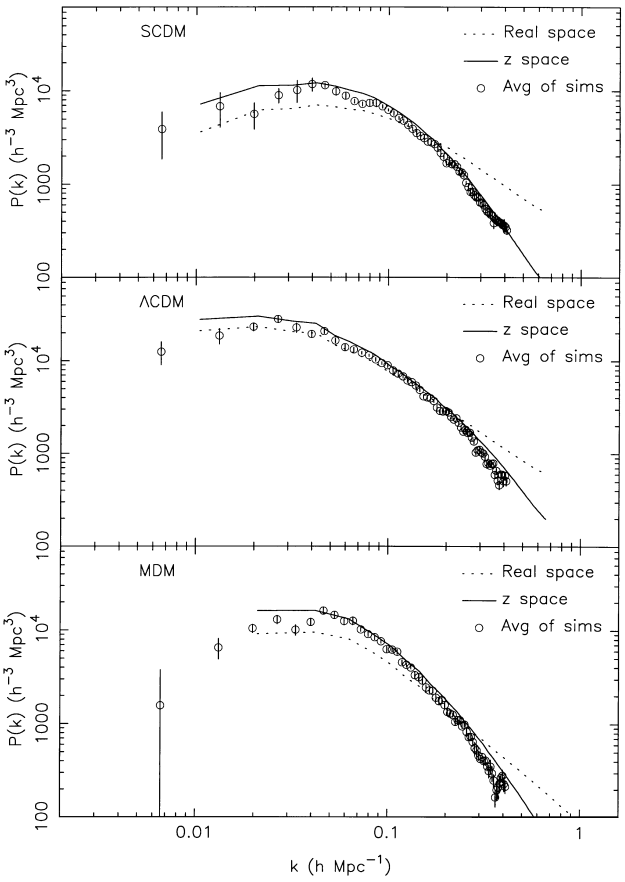

Figure 6. Power spectra for the three models in Table 2. For each model, the dotted and solid lines show the real- and redshift-space power spectrum of the full simulation box (mean of nine runs, error bars negligible). The circles show the mean of the estimated power spectra from nine simulated 'PSCz' surveys, with 1σ error on the mean.

computed their power spectra as above. The three models are 'standard' CDM (SCDM), CDM with a cosmological constant (ΛCDM), and a mixed cold + hot dark matter model (MDM); the simulations use a P3M code (Croft & Efstathiou 1994) and their parameters are listed in Table 2. We place an 'observer' at a random location in the cube, wrap the simulation using periodic boundary conditions, and then select 'galaxies' in redshift space as random particles using the selection function of equation (2) and a 'mask' of the same shape as the real PSCz mask. We generated a total of 27 simulated 'PSCz' surveys for each model; for each model we used nine different runs of the P3M code, and three different observer locations for each run.

Fig. 6 shows the power spectra of the full box for each simulation, compared with results from nine simulated PSCz surveys. As expected, our estimator $\widehat{P}(k)$ recovers the 'true' redshift-space power spectrum quite well for $k \gtrsim 0.02\,h\,\mathrm{Mpc}^{-1}$; the simulated surveys slightly underestimate the true redshift-space $P(k)$ on intermediate scales because of the convolution with the survey window function, but the effect is small. Fig. 7 shows the mean of the FKP error bars from nine simulations (triangles), compared with

Table 1. Estimated power spectrum $\widehat{P}(k)$ with weight $P_\mathrm{e} = 8000\,h^{-3}\,\mathrm{Mpc}^3$, and associated 1σ errors. These data points have been 'corrected' for finite-size bins using equation (10) with $l = 950/128\,h^{-1}\,\mathrm{Mpc}$. Covariances between consecutive entries are substantial for small k but negligible for $k \gtrsim 0.1\,h\,\mathrm{Mpc}^{-1}$.

k ($h\,\mathrm{Mpc}^{-1}$)	$\widehat{P}(k)$ ($h^{-3}\mathrm{Mpc}^3$)	Error	k ($h\,\mathrm{Mpc}^{-1}$)	$\widehat{P}(k)$ ($h^{-3}\,\mathrm{Mpc}^3$)	Error
0.0066	16110	21200	0.0839	8690	1165
0.0132	3981	5774	0.1056	4548	625
0.0198	3503	4039	0.1329	3786	425
0.0265	13514	5960	0.1674	2591	285
0.0334	14189	4861	0.2107	1466	193
0.0420	12459	3428	0.2653	1122	151
0.0529	10241	2321	0.3339	748	119
0.0666	8059	1488	0.4204	545	89

Table 2. *N*-body simulation parameters.

Name	N	Box (h^{-1} Mpc)	$\Omega_{\rm CDM}$	$\Omega_{\rm HDM}$	Ω_Λ	h	σ_8
SCDM	160^3	600	1	0	0	0.5	1.0
ΛCDM	160^3	600	0.2	0	0.8	1.0	1.0
MDM	100^3	300	0.7	0.3	0	0.5	0.67

the 'real' uncertainty estimated from the rms scatter between the nine simulations (crosses). Clearly the FKP error estimates are a reasonable approximation to the 'real' errors in $\widehat{P}(k)$, though they appear to underestimate the actual errors by ∼20 per cent.

In Fig. 8 we compare the data to the mean of 27 simulated PSCz surveys for each model. We find that all three models give a reasonable match to the shape of the observed power spectrum; the ΛCDM model has somewhat too high an amplitude and would require an antibias $b < 1$. However, this could be remedied by lowering h somewhat and raising Ω_0, keeping Γ constant; this would reduce the implied σ_8 for *COBE* normalization, and improve the fit. Alternatively, a modest degree of 'tilt' with primordial spectral index $n < 1$ would similarly reduce the *COBE*-normalized σ_8.

Although the SCDM model has much less large-scale power than the others in real space, the high *COBE* normalization gives two effects: an enhancement of power on large scales by a factor ≈1.86 from the Kaiser (1987) redshift-space distortion, and a suppression of small-scale power from the resulting large peculiar velocities. These two effects combine to bring the redshift-space $P(k)$ of this model into rather good agreement with the data. These effects for *COBE*-normalized SCDM have been previously noted by various authors, e.g. Bahcall, Cen & Gramann (1993), although of course this model has serious problems with cluster abundances (Eke, Cole & Frenk 1996), large-separation gravitational lenses (Cen et al. 1994), etc.

5 DISCUSSION

5.1 Comparison with other surveys

Our observed redshift-space power spectrum for $P_{\rm e} = 8000\,h^{-3}\,{\rm Mpc}^3$ is compared with a number of previous measurements in Fig. 9. These come from various catalogues, both optical and *IRAS*-selected; all are redshift-space power spectra except for the APM data which come from an inversion of the 2D power spectrum. We see that on large scales our measurements are well within the range of previous surveys, but on intermediate scales $\sim 0.2\,h\,{\rm Mpc}^{-1}$ our measurements are slightly steeper than the others, notably the combined QDOT and 1.2-Jy surveys. This is the cause of the low values of $\Gamma \sim 0.2$ for best-fitting CDM-like models seen in the next section. It appears that optical galaxies have

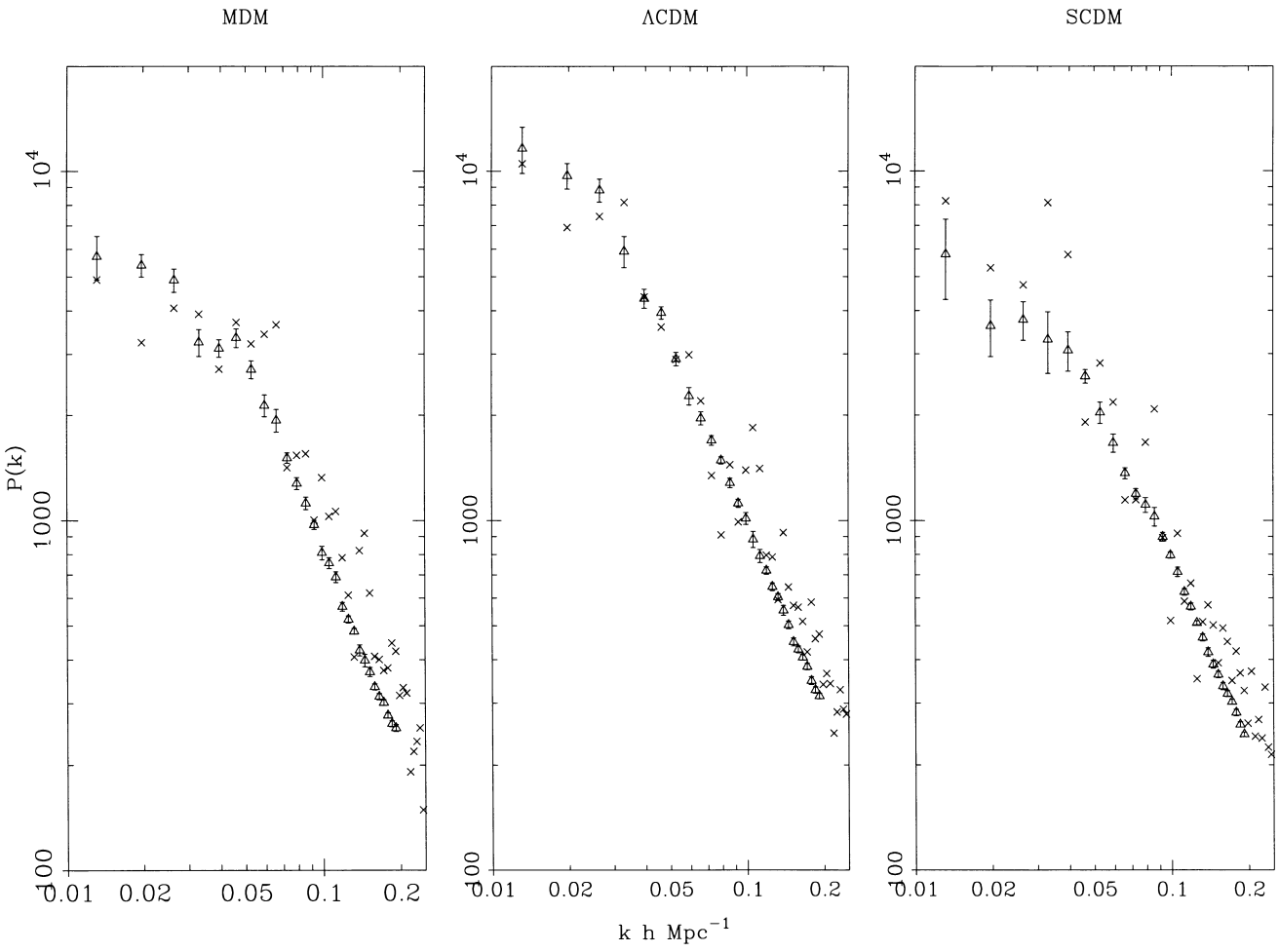

Figure 7. Error estimates for simulated PSCz surveys, with the observed mask and selection function, for the three models in Table 2. Triangles show the mean of the FKP error estimate $\delta\widehat{P}(k)$ from nine simulated surveys; crosses show the 'true' error in $\widehat{P}(k)$ estimated from the scatter in the nine simulated surveys.

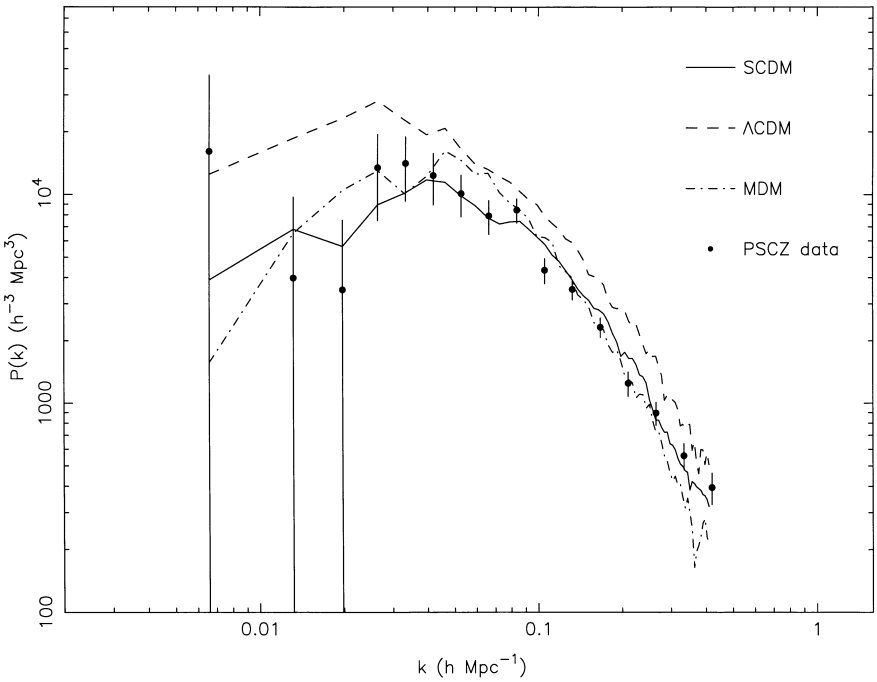

Figure 8. The observed PSCz power spectrum (points with 1σ errors) compared to the mean power spectrum of 27 simulated PSCz surveys for each of the three models (lines).

a somewhat higher power spectrum amplitude on intermediate scales, as expected from the fact that IR-selected surveys contain mainly late-type galaxies, and from their smaller correlation length r_0, but it remains unclear whether this persists to large scales; a direct comparison with APM is complicated by the redshift-space distortion, and the interpretation of Las Campanas is somewhat complicated by the inversion from the 2D to 3D power spectrum caused by the slice-like geometry. Future large optical surveys such as 2dF and Sloan should greatly clarify this question.

5.2 Fits to the power spectrum

In addition to the direct comparison with simulations, it is interesting to extract best-fitting values for parametrized models of the power spectrum; we use first linear theory for simplicity, and later the fitting formulae of Peacock & Dodds (1996), which account both for non-linear evolution of clustering and the effect of distortions between real space and redshift space.

We use CDM-like models with the initial power spectrum

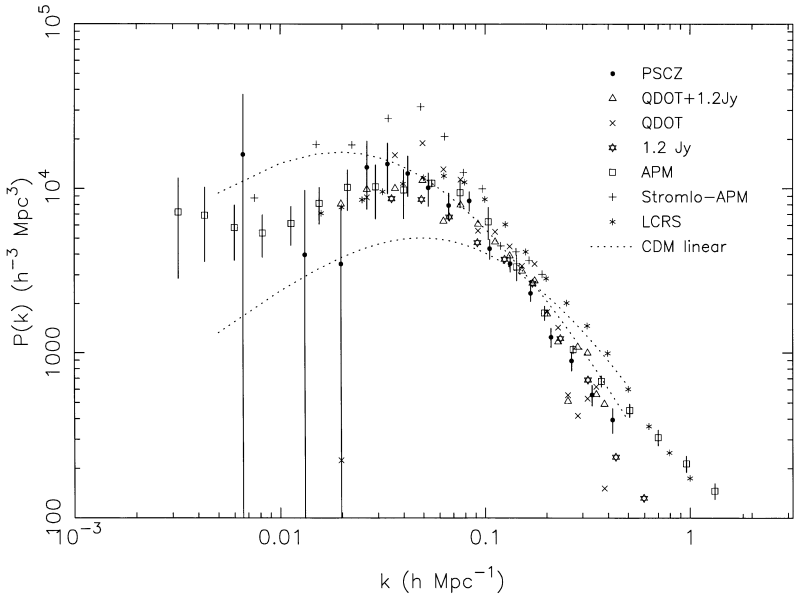

Figure 9. Comparison of PSCz $\widehat{P}(k)$ with other measured power spectra. The data points as labelled on the figure are *IRAS* 1.2-Jy from Fisher et al. (1993), QDOT from FKP, QDOT + 1.2-Jy from Tadros & Efstathiou (1995), Stromlo-APM from Tadros & Efstathiou (1996), APM (real-space, deconvolved) from Baugh & Efstathiou (1994), and Las Campanas (deconvolved) from Lin et al. (1996). For clarity, error bars are only shown on PSCz and APM (others are larger), and Stromlo, QDOT and QDOT+1.2-Jy data have been rebinned. Dotted lines show linear-theory CDM with $\Gamma = 0.2$ and 0.5 with $\sigma_8 = 0.8$.

parametrized by Γ as in equation (7) of Efstathiou, Bond & White (1992, hereafter EBW), which is

$$P(k) = \frac{Bk}{\left\{1 + [ak + (bk)^{3/2} + (ck)^2]^{\nu}\right\}^{2/\nu}}, \quad (11)$$

$$a = 6.4/\Gamma\, h^{-1}\,\mathrm{Mpc}, \quad b = 3.0/\Gamma\, h^{-1}\,\mathrm{Mpc},$$

$$c = 1.7/\Gamma\, h^{-1}\,\mathrm{Mpc}, \quad \nu = 1.13.$$

In linear theory there are only two free parameters: the shape parameter Γ, and the normalization, which may be taken as $b\sigma_8$, where b is the bias parameter and σ_8 is the rms mass fluctuation in an $8\,h^{-1}$ Mpc top-hat sphere. The χ^2 contours using the full covariance matrix are shown in Fig. 10; the best-fitting values are $\Gamma = 0.19 \pm 0.03$ and $b\sigma_8 = 0.80 \pm 0.02$. These compare to $\Gamma = 0.19 \pm 0.06$, $b\sigma_8 = 0.87 \pm 0.07$ for the QDOT survey, as given by FKP equation (4.3.3).

For the non-linear Peacock–Dodds formula, we need a total of six parameters to specify the present-day redshift-space power spectrum: the initial mass power spectrum is specified as above by Γ and σ_8 (where σ_8 is defined as the *initial* rms mass fluctuation, multiplied by the linear-theory growth factor to the present day). The subsequent non-linear evolution depends also on Ω_0 and (weakly) on Ω_Λ. The transformation from real to redshift space depends on Ω_0 and the bias b, and also on the pairwise peculiar velocity dispersion; in the Peacock–Dodds formula this is approximated by assuming galaxy velocities are independent Gaussians with dispersion $\sigma_V = \sqrt{v_{12}^2(r)/2}$ for some suitable scale r. We assume simple 'linear bias' so the galaxy power spectrum is $b^2\times$ the matter power spectrum. There is clearly insufficient information in the $P(k)$ data to fit all six parameters separately, so we restrict the parameter space as follows.

(i) To set Ω, we consider either Einstein–de Sitter models, with $\Omega = 1, \Omega_\Lambda = 0$, treating Γ as a free parameter (which is a reasonable approximation to e.g. mixed dark matter models); or we consider ΛCDM models with $\Omega = \Gamma/0.66$, $\Omega_\Lambda = 1 - \Omega$ (i.e. assuming $\Gamma = \Omega h$ with a Hubble constant $h = 0.66$, consistent with most recent measurements).

(ii) To set σ_8, we use either the cluster normalization $\sigma_8 = 0.52\Omega^{(-0.52+0.13\Omega)}$ (Eke et al. 1996), or we use *COBE* normalization where σ_8 is a function of Γ using equation (6) of EBW and $Q_{\rm rms} = 17\,\mu$K.

(iii) To set σ_V, we fix either $\sigma_V = 300$ or $600\,\mathrm{km\,s^{-1}}$, or predict σ_V as a function of Γ, σ_8 using the fitting formula in equations (40a) and (40b) of Mo, Jing & Borner (1997, hereafter MJB). A value as high as $600\,\mathrm{km\,s^{-1}}$ is probably disfavoured by observations (Landy, Szalay & Broadhurst 1998), but we include this as a conservative upper limit to show the effect on the derived parameters.

Having made one choice from each of (i), (ii), (iii) above, this defines $\Omega, \Omega_\Lambda, \sigma_8, \sigma_V$ as a function of Γ; we then treat Γ and b as free parameters, and fit to the observed $\widehat{P}(k)$ data. We choose to use only the data points in the range $0.021 < k < 0.3\,h\,\mathrm{Mpc}^{-1}$ in the fits, since points at lower k may be affected by the convolution, and those at higher k are subject to large and somewhat uncertain corrections both for the peculiar velocity term and the binning correction of equation (10).

The best-fitting values of $\Gamma, b\sigma_8$ for each of the above parameter choices are shown in Table 3. [We present the fit results in terms of $(\Gamma, b\sigma_8)$ rather than (Γ, b) because b and σ_8 are degenerate in the linear regime, and also for simplicity since the contours of equal χ^2 are roughly parallel to the axes in the $(\Gamma, b\sigma_8)$ plane.] For the low-Ω cluster-normalized case, contours of goodness of fit are shown in Fig. 10 for each of the three σ_V assumptions. The derived power spectra for the best fits in the same cases are shown in Fig. 11. For most of the fits, a fairly small value of $\Gamma \sim 0.2$ is favoured, and $\Gamma \sim 0.5$ is quite strongly ruled out; for the cases with $\sigma_V = 600\,\mathrm{km\,s^{-1}}$, higher values $\Gamma \sim 0.35$ are favoured and $\Gamma = 0.5$ is only marginally ruled out, though values of σ_V as high as this are definitely not favoured observationally.

Table 3. Fits of CDM-like models to the observed $\widehat{P}(k)$ in the $(\Gamma, b\sigma_8)$ plane. The first line shows linear theory, the remainder use the non-linear PD formula, using various choices for setting the other input parameters $(\Omega, \Omega_\Lambda, \sigma_8, \sigma_V)$ as a function of Γ. Column 1: either $\Omega = 1, \Omega_\Lambda = 0$ or $\Omega = 0.66/\Gamma, \Omega_\Lambda = 1 - \Omega$; Column 2: σ_8 defined either by *COBE* or cluster normalization; Column 3: σ_V either fixed to 300 or $600\,\mathrm{km\,s^{-1}}$, or defined as a function of the other parameters using the MJB model. For the σ_8 and σ_V columns, the values in brackets show the derived values at the best-fitting Γ. The * in the last column flags the models plotted in Figs 10 and 11.

Ω	Norm (σ_8)	$\sigma_V(\mathrm{km\,s^{-1}})$	Γ	$b\sigma_8$	Plot?
Linear	–	–	0.19	0.80	*
1	*COBE* (0.45)	300	0.20	0.67	
1	*COBE* (0.49)	MJB (368)	0.22	0.68	
1	*COBE* (1.00)	600	0.40	0.71	
1	Clus (0.52)	300	0.20	0.66	
1	Clus (0.52)	MJB (390)	0.23	0.69	
1	Clus (0.52)	600	0.34	0.81	
Γ/0.66	*COBE* (0.97)	300	0.16	0.66	
Γ/0.66	*COBE* (0.97)	MJB (457)	0.16	0.70	
Γ/0.66	*COBE* (1.38)	600	0.34	0.73	
Γ/0.66	Clus (0.91)	300	0.20	0.67	*
Γ/0.66	Clus (0.81)	MJB (438)	0.25	0.74	*
Γ/0.66	Clus (0.73)	600	0.31	0.83	*

There is little difference between the goodness-of-fit for the various choices, though the fits for $\sigma_V = 600\,\mathrm{km\,s^{-1}}$ are somewhat worse. For a given parameter choice, the 1σ random errors are typically ± 15 per cent in Γ and ± 4 per cent in $b\sigma_8$. In general we see that the systematic uncertainties from the different choices of $\Omega, \sigma_8, \sigma_V$ dominate the random errors arising from the error bars on $\widehat{P}$; the largest source of uncertainty is that arising from σ_V. As expected, if we increase σ_V the predicted small-scale power decreases at a fixed Γ, and thus the best-fitting values of Γ and $b\sigma_8$ increase to compensate.

For ΛCDM models, the value of Γ at which the *COBE* and cluster normalizations agree is $\Gamma = 0.17, \sigma_8 \approx 1.0$; this is interestingly close to our best-fitting values of $\Gamma \sim 0.2$. Our fit values of $b\sigma_8$ thus imply $b \sim 0.75$: this is a significant amount of 'antibias', but may be plausibly accounted for by the deficiency of *IRAS* galaxies in rich clusters. Thus a ΛCDM model is attractive in that it can simultaneously satisfy three constraints [*COBE*, cluster abundance, $P(k)$] with one free parameter Γ, if optical galaxies are approximately unbiased and *IRAS* galaxies mildly antibiased relative to the mass.

5.3 Periodicities and spikes

There have been a number of suggestions of a 'preferred scale' for large-scale clustering, notably by Broadhurst et al. (1990), Landy et al. (1996) and Einasto et al. (1997). These effects, if real, could arise from a 'spike' in the power spectrum, such as may arise from a baryon isocurvature model or non-standard inflation models, or from non-Gaussian initial conditions, which could lead to one particular direction showing a value of $|\delta(\boldsymbol{k})|^2$ much larger than

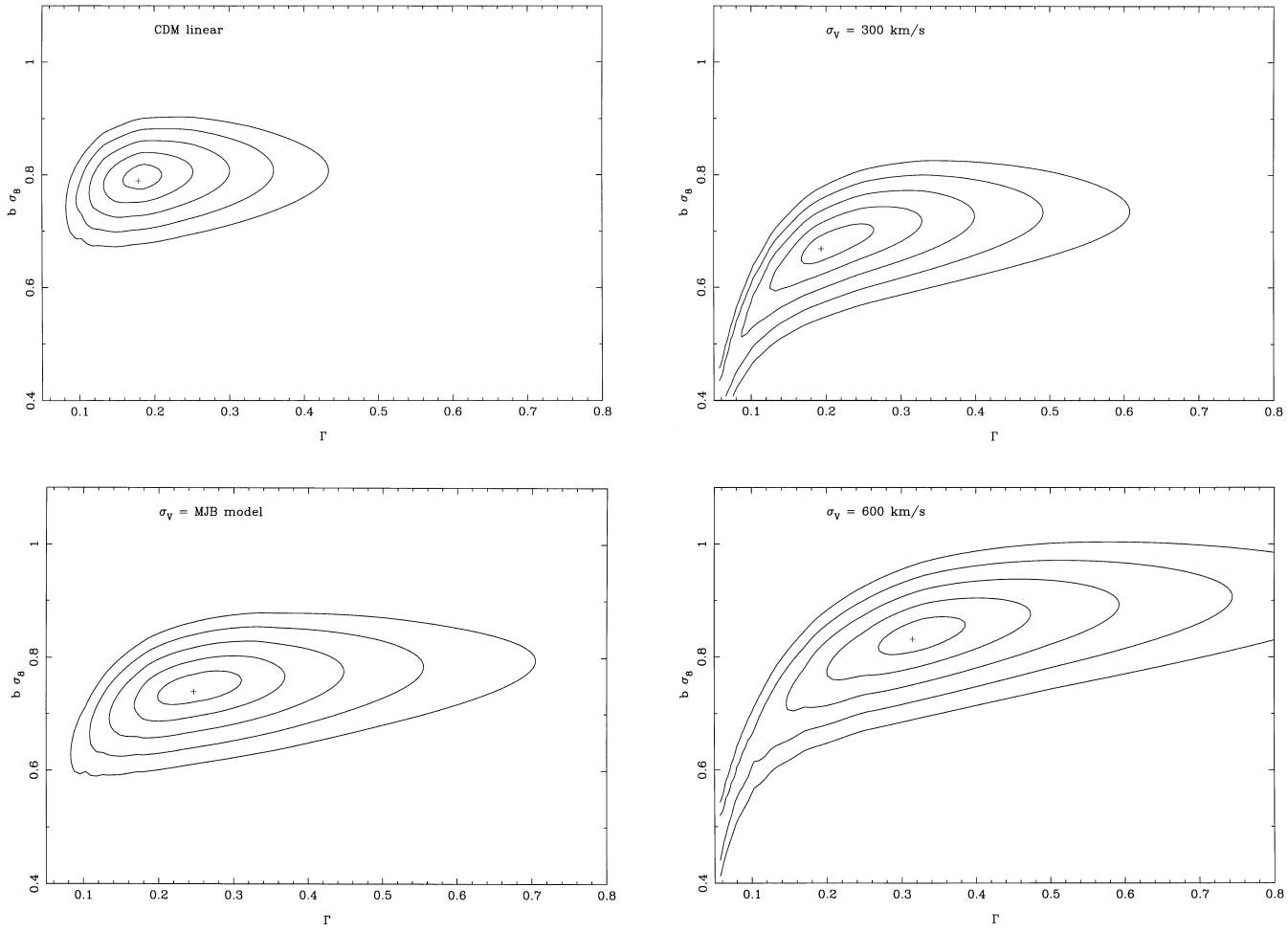

Figure 10. Contours of χ^2 in the $(\Gamma, b\sigma_8)$ plane for fits to the observed power spectrum. The upper left panel shows linear theory. Other panels use the Peacock–Dodds formula as in Section 5.2, with $\Omega = \Gamma/0.66$, cluster normalization, and different choices of random velocities σ_V as labelled. The cross denotes the minimum χ^2, contours are at $\chi^2 = \chi^2_{\rm min} + 1, 4, 9, 16, 25$.

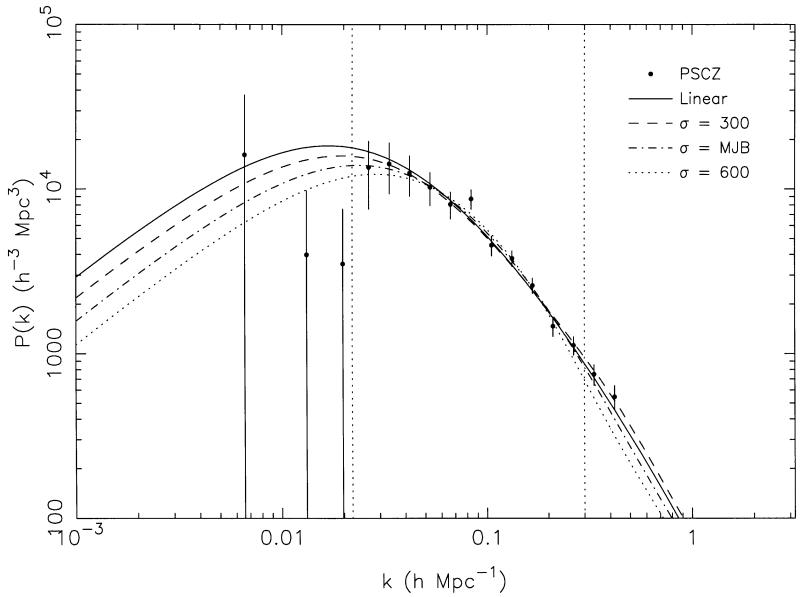

Figure 11. Fits to the measured power spectrum (points) using the Peacock–Dodds formula as in Section 5.2. Vertical dotted lines denote the range of k used in the fits. Lines show the fitted power spectra as labelled, one for linear theory and three for different values of σ_V, for the case of a low-density universe with $\Omega = \Gamma/0.66$, and cluster normalization.

its expectation value $P(k)$, or even from an intrinsic 'preferred direction' in the Universe.

In our data, there is marginal evidence for a 'spike', perhaps better described as a 'step', in the power spectrum near $k \sim 0.08\,h\,\mathrm{Mpc}^{-1}$, but this is only about a 2σ effect above a smooth CDM-like fit, and the scale is significantly different from that ($k \sim 0.06\,h\,\mathrm{Mpc}^{-1}$) suggested by Broadhurst et al. (1990) and Landy et al. (1996); also, we find that changing our flux limit to $f_{60} > 0.7$ Jy causes a substantial drop in $\widehat{P}(k)$ at this point, while leaving other points virtually unchanged. Thus, we suspect this point may be a statistical fluctuation, and there is no conclusive evidence for a feature in our power spectrum. From inspection of results from a number of realizations of N-body simulations, we find that such features quite commonly arise from statistical fluctuations.

To test for non-Gaussian effects, we have examined the histogram of the ratio of observed to mean power, $|F(\boldsymbol{k})|^2/(P(k) + P_{\rm shot})$, for each wavenumber; for Gaussian clustering, this should follow an exponential distribution with unit mean. Results for several ranges of wavenumber are shown in Fig. 12, and closely follow the exponential distribution. The presence of the shot noise somewhat weakens this test, since for smaller scales $P_{\rm shot} \gtrsim P(k)$, but at large scales this is a sensitive test for non-Gaussian initial conditions with a 'tail' to high values. The distributions are well fitted by the exponential, so there is no evidence for non-Gaussian initial conditions or any 'preferred direction' in our survey.

This also strongly constrains any 'preferred direction', as follows. If there exists a strict plane-wave periodicity in the Universe with dimensionless density contrast a along wavevector $\boldsymbol{k}_0$, the true power spectrum contains delta functions at $\pm\boldsymbol{k}_0$, $P(\boldsymbol{k}) = C[\delta(\boldsymbol{k} - \boldsymbol{k}_0) + \delta(\boldsymbol{k} + \boldsymbol{k}_0)]$. Requiring the variance $\sigma^2 = a^2/2 = (2\pi)^{-3} \int \mathrm{d}^3k\, P(\boldsymbol{k})$ gives the constant $C = (2\pi)^3 a^2/4$. Then, after convolution with the survey window function as in equation (7), this contributes to the observed power spectrum a term of size

$$\widehat{P}_{\rm spike}(\boldsymbol{k}) = \frac{a^2}{4}\left[|G(\boldsymbol{k} - \boldsymbol{k}_0)|^2 + |G(\boldsymbol{k} + \boldsymbol{k}_0)|^2\right]. \tag{12}$$

Recall that

$$|G(k=0)|^2 = \frac{\left[\int \mathrm{d}^3r\, \overline{n}(\boldsymbol{r}) w(\boldsymbol{r})\right]^2}{\int \mathrm{d}^3r\, \overline{n}^2(\boldsymbol{r}) w^2(\boldsymbol{r})}\,; \tag{13}$$

for a volume-limited survey with constant $\overline{n}, w$ this just reduces to the survey volume V, so it may be thought of as the survey 'effective volume'. For our survey with weight function given by $P_{\rm e} = 8000\,h^{-3}\,\mathrm{Mpc}^3$, we have $|G(0)|^2 = 6.2 \times 10^7\,h^{-3}\,\mathrm{Mpc}^3$: thus even a small-amplitude periodic wave of $a = 0.15$ would lead to a large spike in our measured $\widehat{P}(\boldsymbol{k}_0) \approx 3 \times 10^5\,h^{-3}\,\mathrm{Mpc}^3$, well outside the exponential tail of measured values. We conclude that there is no strictly periodic plane-wave structure in our survey volume with amplitude larger than 15 per cent.

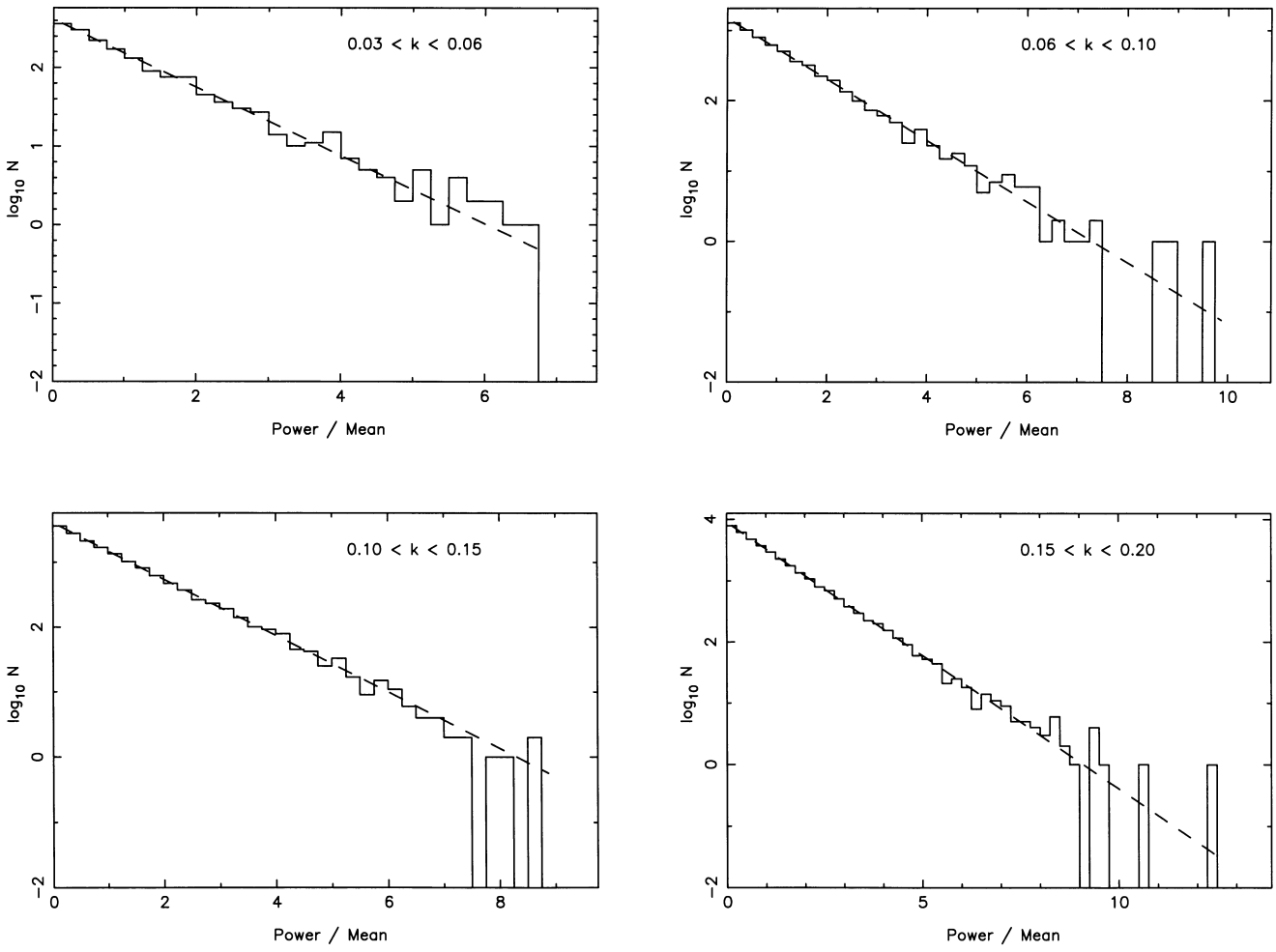

Figure 12. Solid lines show histograms of 'observed' power $\widehat{P}(\boldsymbol{k}) + P_{\rm shot}$ divided by the mean for each k. The dashed line shows an exponential distribution with unit mean. The four panels show various ranges in k as labelled.

6 CONCLUSIONS

Our conclusions may be summarized as follows.

(i) The redshift-space power spectrum of the PSCz survey is intermediate between those of the earlier QDOT and 1.2-Jy *IRAS* surveys on large scales, though it is slightly steeper on small scales. It is stable against variations in the galactic cuts and redshift limits etc., though the amplitude decreases slightly for a flux cut $f \gtrsim 0.8$ Jy.

(ii) There is convincing evidence for curvature in the power spectrum; the slope changes from the small-scale power law $n \approx -1.4$ to $n \sim 0$ on scales $k \lesssim 0.07\,h\,\mathrm{Mpc}^{-1}$. This is not an artefact of the finite sample volume or the estimation of the mean density from the survey.

(iii) The best-fitting CDM-like models have $\Gamma \sim 0.25, b\sigma_8 \sim 0.7$. The uncertainties in these values are mainly caused by uncertainties in the small-scale velocity dispersion, the value of Ω etc., rather than statistical errors.

(iv) There is little evidence for a 'spike' in the power spectrum, and no evidence for large-scale periodicity or non-Gaussianity.

ACKNOWLEDGMENTS

We are very grateful to many observers, especially Marc Davis, Tony Fairall, Karl Fisher and John Huchra, for supplying redshifts in advance of publication. We thank the staff at the INT, AAT and CTIO telescopes for support, especially Hernan Tirado and Patricio Ugarte at CTIO. WSu is supported by a PPARC Advanced Fellowship. WSa is supported by a Royal Society Fellowship. GE thanks PPARC for the award of a Senior Fellowship.

REFERENCES

Bahcall N. A., Cen R., Gramann M., 1993, ApJ, 408, L77
Baugh C. M., Efstathiou G., 1993, MNRAS, 265, 145
Baugh C. M., Efstathiou G., 1994a, MNRAS, 267, 323
Baugh C. M., Efstathiou G., 1994b, MNRAS, 270, 183
Beichman C. A., Neugebauer G., Habing H. J., Clegg P. E., Chester T. J., 1988, NASA Reference Pub. 1190, Vol. 1, Infrared Astronomical Satellite (*IRAS*) Catalogs and Atlases. NASA, Washington DC
Branchini E. et al., 1999, MNRAS, 308, 1
Broadhurst T. J., Ellis R. S., Koo D., Szalay A., 1990, Nat, 343, 726
Canavezes A. et al., 1998, MNRAS, 297, 777
Cen R., Gott J. R., Ostriker J. P., Turner E. L., 1994, ApJ, 423, 1
Cole S., Hatton S., Weinberg D. H., Frenk C. S., 1998, MNRAS, 300, 945
Croft R. A. C., Efstathiou G., 1994, MNRAS, 268, L23
Efstathiou G., 1995, MNRAS, 276, 1425
Efstathiou G., Bond J. R., White S. D. M., 1992, MNRAS, 258, 1P (EBW)
Einasto J. et al., 1997, Nat, 385, 139
Eke V. R., Cole S., Frenk C. S., 1996, MNRAS, 282, 263
Feldman H. A., Kaiser N., Peacock J. A., 1994, ApJ, 426, 23 (FKP)
Fisher K. B., Davis M., Strauss M. A., Yahil A., Huchra J. P., 1993, ApJ, 402, 42
Fisher K. B., Huchra J. P., Strauss M. A., Davis M., Yahil A., Schlegel D., 1994, ApJS, 100, 69
Fry J. N., Gaztanaga E., 1993, ApJ, 413, 447
Hamilton A. J. S., 1996, in Maurogordato S. et al., eds, Proc. XXXth Rencontres Moriond, Clustering in the Universe. Editions Frontieres, Gif-sur-Yvette, p. 143
Kaiser N., 1987, MNRAS, 227, 1
Landy S. D., Shectman S. A., Lin H., Kirshner R. P., Oemler A., Tucker D. L., 1996, ApJ, 456, L1
Landy S. D., Szalay A. S., Broadhurst T. J., 1998, ApJ, 494, L133
Lawrence A. et al., 1998, MNRAS, in press
Lin H., Kirshner R. P., Shectman S. A., Landy S. D., Oemler A., Tucker D. L., Schechter P. L., 1996, ApJ, 471, 617
Maddox S. J., Efstathiou G., Sutherland W. J., 1996, MNRAS, 283, 1227
Mann R. G., Peacock J. A., Heavens A. F., 1998, MNRAS, 293, 209
Mo H. J., Jing Y.-P., Borner G., 1997, MNRAS, 286, 979 (MJB)
Park C., Vogeley M., Geller M. J., Huchra J. P., 1994, ApJ, 431, 569
Peacock J. A., Dodds S., 1996, MNRAS, 280, L19
Peacock J. A., Nicholson D., 1991, MNRAS, 253, 307
Peebles P. J. E., 1980, The Large-Scale Structure of the Universe. Princeton Univ. Press, Princeton NJ
Rowan-Robinson M., Saunders W., Lawrence A., Leech K., 1991, MNRAS, 253, 485
Saunders W. et al., 1996, in Aragon-Salamanca A., Maddox S., eds, Wide-Field Spectroscopy and the Distant Universe. World Scientific, Singapore
Springel V., White S. D. M., 1998, MNRAS, 298, 143
Tadros H., Efstathiou G., 1995, MNRAS, 276, L45
Tadros H., Efstathiou G., 1996, MNRAS, 282, 1381
Tadros H., Efstathiou G., Dalton G., 1998, MNRAS, 296, 995
Tadros H. et al., 1999, MNRAS, in press
Tegmark M., 1995, ApJ, 455, 429
Tegmark M., Hamilton A. J. S., Strauss M. A., Vogeley M., Szalay A., 1998, ApJ, 499, 555

APPENDIX A: NORMALIZATION OF $P(k)$

We note an issue concerning the overall normalization of $P(k)$. FKP set a normalization of their weight function via their equation (2.4.1). It is convenient in practice to set weights via equation (1) with $A = 1$, and then later divide all power spectra by a constant A. There are several ways of doing this, which give similar but not identical results: The left-hand side of FKP's equation (2.4.1) gives

$$A_1 = \int \mathrm{d}^3 r\, \overline{n}^2(r) w^2(r); \tag{A1}$$

the right-hand side gives

$$A_2 = \alpha \sum_{\mathrm{s}} \overline{n}(r_{\mathrm{s}}) w^2(r_{\mathrm{s}}), \tag{A2}$$

where the sum runs over random points, and $\alpha = N_{\mathrm{g}}/N_{\mathrm{r}}$ as before. Another possible definition is

$$A_3 = \frac{\alpha^2}{v}\left(\sum_{\mathrm{cells}} c_i^2 - \sum_{\mathrm{s}} w_i^2\right), \tag{A3}$$

where the first sum runs over the cells used in the Fourier transform, c_i is the sum of weights of all random points in the ith cell and v is the volume of a unit cell. [This results from estimating the window function from the fast Fourier transform of the random points via

$$|\widehat{G}(\boldsymbol{k})|^2 = \frac{\alpha^2}{A_3 V}\left(\left|\sum_{\mathrm{cells}} c_i \mathrm{e}^{i\boldsymbol{k}.\boldsymbol{r}_i}\right|^2 - \sum_{\mathrm{s}} w_i^2\right)\ ; \tag{A4}$$

requiring $\sum_{\boldsymbol{k}} |\widehat{G}(\boldsymbol{k})|^2 = 1$ leads to equation (A3).]

The relationship between A_1, A_2, A_3 is as follows: the number of random points N_{r} is arbitrarily fixed, and we define $\beta = \int \mathrm{d}^3 r\, \overline{n}(r)/N_{\mathrm{r}}$ to be the ratio of the *expected* number of galaxies from the selection function to the number of random points, which should be similar to but not identical to α. Thus the expected number of randoms in cell i is just $\overline{n}_i v/\beta$ where $\overline{n}_i \equiv \overline{n}(\boldsymbol{r}_i)$. For small cells, all randoms in a given cell will have equal weight w_i, thus $c_i = w_i \times \mathrm{Poisson}(\overline{n}_i v/\beta)$. Thus

$$\begin{aligned}\langle A_2\rangle &= \alpha \sum_{\mathrm{cells}} \langle c_i\rangle \overline{n}_i w_i^2 \\ &= \alpha \sum_{\mathrm{cells}} \overline{n}_i^2 v w_i^2/\beta = \frac{\alpha}{\beta} A_1.\end{aligned} \tag{A5}$$

Since c_i is a Poisson variable multiplied by w_i, $\langle c_i^2\rangle = w_i^2[(\overline{n}_i v/\beta)^2 + \overline{n} v/\beta]$, thus equation (A3) gives

$$\langle A_3\rangle = \frac{\alpha^2}{v}\left(\frac{v^2}{\beta^2}\sum_{\rm cells} w_i^2\overline{n}_i^2 + \frac{v}{\beta}\sum_{\rm cells} w_i^2\overline{n}_i - \sum_{\rm cells}(\overline{n}_i v/\beta)w_i^2\right) = \frac{\alpha^2 v}{\beta^2}\sum_{\rm cells} w_i^2\overline{n}_i^2 = \frac{\alpha^2}{\beta^2}A_1. \quad \text{(A6)}$$

Thus we see that the three definitions of A differ by powers of α/β, which is just the ratio of 'observed' to 'expected' number of galaxies. Which is more 'correct' is largely a matter of choice, but the definition A_3 is convenient in practice since it leaves the results unchanged if we rescale the selection function by a constant $\overline{n} \rightarrow c\overline{n}$ and rescale the weights by $P_{\rm e} \rightarrow P_{\rm e}/c$.

This paper has been typeset from a TEX/LATEX file prepared by the author.